Physics of Fluids

RESEARCH ARTICLE | AUGUST 05 2024

Development of a multiple laser-sheet imaging technique for the analysis of three-dimensional turbulent explosion flame structures

Pervez Ahmed ; Benjamin John Alexander Thorne ; Junfeng Yang

Physics of Fluids 36, 085112 (2024)
https://doi.org/10.1063/5.0207937

AIP Publishing

Development of a multiple laser-sheet imaging technique for the analysis of three-dimensional turbulent explosion flame structures

Cite as: Phys. Fluids **36**, 085112 (2024); doi: 10.1063/5.0207937
Submitted: 12 March 2024 · Accepted: 28 June 2024 ·

Pervez Ahmed, Benjamin John Alexander Thorne, and Junfeng Yang[a)]

AFFILIATIONS

University of Leeds, School of Mechanical Engineering, Leeds LS2 9JT, United Kingdom

[a)]Author to whom correspondence should be addressed: J.Yang@leeds.ac.uk

ABSTRACT

The present work describes the development of a multiple laser-sheet imaging technique for the study of turbulent, premixed flame surface structures at high Karlovitz stretch factor values. Experiments were conducted using CH_4 air mixtures at 365 K and 0.5 MPa and up to a root mean square turbulence velocity of 1.5 m/s. A high-speed Nd:YAG laser capable of pulsing up to 60 kHz in conjunction with a high-speed camera and a rotating mirror was used to reconstruct time-resolved three-dimensional turbulent flames. This has, for the first time, enabled the direct measurement of wrinkled flame surface areas, along with reaction progress variable and flame brush thickness. These are important parameters for the characterization of turbulent burning rates and provide more insight into the dynamic nature of the flames and their structures. In addition, the current data aid toward direct comparison with results from combustion simulation studies.

NOMENCLATURE

A	total flame surface area (mm^2)
A_m	half the distance between RM parallel faces
a_i	geometric offset of each IL sheet from the centerline of the CV
a_m, a_v	mean flame area based on mass and volume balancing
$\bar{c}$, $\bar{c}_{Rj}$	reaction progress variable, reaction progress variable at radius R_j
f	focal length (mm), mass fraction of burned gas
f_L	effective focal length (mm)
f_{IL}	imaging laser frequency
i	independent variable
I1, R1, N1, R2, N2	incident ray, reflected ray, normal at time t_0 and reflected ray, normal after RM rotation by angle θ_m
K	Karlovitz stretch factor
L	integral length scale (mm)
Ma_{sr}	Markstein number for strain rate
N_f	fan rotating speed (rpm)
n_f	number of RM faces
P	pressure (MPa)
r	radius of the flame kernel
r_m, r_v	mean flame radius based on mass and volume balancing
R_L	turbulent Reynolds number based on turbulent integral length scale
R_r, R_t, R_j	root, tip, and variable radius, respectively
T	unburned gas temperature (K)
t_s	time between two sweeps
t_{sIL}	time between two *IL* successive sheets
t_0	initial time
u_t	turbulent burning velocity (m/s)
u'	rms velocity (m/s)
u'_k	effective rms velocity (m/s)
u_l	laminar burning velocity (m/s)
V	total volume of the 3D flame
v_i	volume of voxel with index i
X_m	diagonal distance between the center of the RM face before and after rotation by angle θ_m
Z	distance between the rotating mirror face and the start of plane of interest

Greek

δ_l	laminar flame thickness (mm)
ζ_n	angle made by the ith sheet with the centerline of the CV
θ_m	angle rotated by RM
λ	wavelength of the laser light
ν	kinematic viscosity (m^2/s)
$\sum$	flame surface density
ρ_b	burned gas density (kg/m^3)
ρ_u	unburned gas density (kg/m^3)
ϕ	equivalence ratio
ω	angular rotating frequency of the RM in radians/s

Abbreviations

CV	combustion vessel
CT	computed tomography
DNS	direct numerical simulations
FBE	fiber-based endoscope
I_gL	ignition laser
IL	imaging laser
LES	large eddy simulation
Nd:YAG	neodymium-doped yttrium-aluminum garnet
PLIF	planar laser-induced fluorescence
RM	rotating mirror
VLIF	volumetric laser-induced fluorescence

INTRODUCTION

Immediately following ignition, turbulent flames are only wrinkled by smaller length scales of turbulence, with larger length scales merely convecting the flame; only when the flame grows large enough, will it be susceptible to the bulk of the turbulent length scales available (Abdel-Gayed *et al.*, 1987). The burning rate of a turbulent flame is strongly affected by its flame structure. This is expressed as the turbulent burning velocity, u_t, a term often used in engine combustion and explosion studies. Wrinkling of a turbulent flame affects the total surface area, A, available for reaction, which in turn contributes to u_t (Bradley *et al.*, 2011; Lipatnikov and Chomiak, 2002). Parameters such as reaction progress variable, $\bar{c}$ (Bray *et al.*, 2005), and flame surface density, $\sum$ (Halter *et al.*, 2009), also quantify the effects of wrinkling on the flame structure.

The evaluation of these parameters until recently was largely confined to two-dimensional (2D) sheet imaging techniques in combustion vessels of uniform turbulence. For example, experimental measurements of u_t, $\sum$, and $\bar{c}$ were made (Bagdanavicius *et al.*, 2015; Bradley *et al.*, 2013; Bradley *et al.*, 2009; Bradley *et al.*, 2011; Hult *et al.*, 2007; and Lee *et al.*, 2000) but largely limited to 2D laser-sheet techniques. These studies relied on the assumption that the flame surface detail witnessed in two dimensions was representative of the overall three-dimensional (3D) flame structure. It is often assumed that the average surface area per unit volume equals the average flame perimeter per unit area in the laser sheet to determine $\sum$ (Filatyev *et al.*, 2005). However, the limitation of this technique is that the behavior of flames in the third dimension is not known. Moreover, flames in the early stages of development, particularly lean mixtures/slow laminar burning velocity mixtures, are displaced from the center by larger length scales, thereby increasing the uncertainty of slicing the flame through its center. As a result, the various flame parameters using the 2D techniques could be either underestimated or overestimated depending upon the position of the slicing through the flame.

Modeling of turbulent flames using $\sum$ and $\bar{c}$ has also been carried out extensively in both 2D and 3D by many researchers (Bray and Peters, 1994; Lee *et al.*, 2000; Mantzaras *et al.*, 1988; Nivarti and Cant, 2017; Peters, 1999; and Pole and Cheng, 1988); however, limited experimental data are available to assess the validity of the resulting models. A summary of the 3D experimental work carried out so far is presented in Table I. Various researchers (Hult *et al.*, 2002; Lawes *et al.*, 1998; Nygren *et al.*, 2002; and Yip *et al.*, 1987) have proposed multiple simultaneous laser-sheet imaging to overcome the limitation posed by 2D techniques. Yip *et al.* (1987) used a multiple laser-sheet technique incorporating a rotating mirror, RM, through an aerosol seeded gas jet, to capture successive images of the jet. Mantzaras *et al.* (1988) used a limited number of sheets, typically four, of different wavelengths for instantaneous multiple sheet imaging. However, to create a pseudo-instantaneous 3D flame structure at sufficiently high resolution to capture fine flame surface details, the laser sheets are required to traverse at a very high frequency. Hult *et al.* (2002) applied a similar technique employing a neodymium-doped yttrium-aluminum garnet (Nd:YAG) laser to study flames stabilized on a burner, while Nygren *et al.* (2002) investigated combustion in a homogeneous charge compression ignition (HCCI) engine using a similar setup, with laser-induced fluorescence employed to reveal chemical species as an indicator of extent of combustion. More recently, Upton *et al.* (2011) studied burner flames using computed tomography (CT) with 12 individual detectors equispaced around the flame.

Lawes *et al.* (1998) adopted the methodology of Yip *et al.* (1987) to construct 3D turbulent flames at a faster laser frequency, while the flames were only analyzed recently by Harker *et al.* (2011; 2012). Ng and Zhang (2003) demonstrated stereoscopic imaging and reconstruction of turbulent impinging flames using one camera to capture a pair of stereo images. However, their technique was limited to only lightly wrinkled flames as well as to those flame surfaces visible from two different points (complex flames). The technique also had difficulty in resolving transparent or semi-transparent flames and recommended laser-based techniques to be used. Bheemul *et al.* (2005) developed an optical instrumentation system for the measurement of 3D geometric parameters of gaseous flames in real time using visual hull reconstruction. The visual hull is a geometric shape obtained using silhouettes of flames as seen from a number of views. However, even with a large number of views, the result would not give a real representation of flames. Moreover, these authors' method tends to be restricted to very low-resolution reconstruction of ignition volume and ignition surface areas only. Steinberg *et al.* (2008) used a cinema stereoscopic Particle Image Velocimetry (PIV) technique to resolve the effect of 3D velocity fields on flame wrinkling. These authors showed that the flame contour from particle gradient (Mie-scattering) method corresponds well to the true location of the maximum gas density gradient obtained from CH-PLIF. However, this study indicated that the effect of eddies on the flame wrinkling cannot be resolved using such techniques. Tanahashi *et al.* (2008) reconstructed 3D turbulent premixed flames in a noise-controlled, swirl-stabilized combustor by evaluating mean reaction progress variable using 2D OH-PLIF images. However, the 2D images were averaged over 100 temporal images to evaluate the

TABLE I. Some previous experimental studies of 3D imaging.

Authors	Year	Journal, Ref	Measurement technique	Equipment	Laser pulse energy	Voxel size	Apparatus	Ext info
Yip *et al.*	1987	Science (Yip *et al.*, 1987)	3D, Aerosol concentration measurements	Rotating mirror, 1 camera, thin multiple laser sheet	0.3 μJ		Jet nozzle	30 kHz
Mantzaras *et al.*	1988	SAE (Mantzaras *et al.*, 1988)	Mie-scattering technique	Four laser sheet	150, 100, 40, 5 mJ	0.35 mm	SI engine	
Nygren *et al.*	2002	Proc. Combust. Inst. (Nygren *et al.*, 2002)	Planar laser-induced fluorescence, PLIF, multiple imaging	Scanning mirror	25–30 mJ		HCCI engine	10 Hz
Hult *et al.*	2002	Exp. Fluids (Hult *et al.*, 2002)	Laser-induced incandescence, LII	Scanning mirror	150 mJ		Burner	
Ng and Zhang	2003	Exp. Fluids (Ng and Zhang, 2003)	Stereoscopic imaging	1 camera			Impinging burner	
Bheemul *et al.*	2005	IEEE Trans. Intrum. Meas. (Bheemul *et al.*, 2005)	3D digital imaging	3 monochromatic CCD cameras		0.23 mm × 0.21 mm	Burner	Reported ign. SA
Steinberg *et al.*	2008	Exp. Fluids (Steinberg *et al.*, 2008)	Cinema stereoscopic PIV, 3D velocity fields, CH-PLIF	2 cameras	8 mJ	0.14 mm	Bunsen burner	1 kHz
Tanahashi *et al.*	2008	Exp. Fluids (Tanahashi *et al.*, 2008)	3D flames using 2D CH-OH-PLIF + stereoscopic PIV, OH-PLIF	Multiple planes, 4 cameras		0.023 mm, 0.05 mm	Swirl burner	
Mason *et al.*	2009	Fire Technol. (Mason *et al.*, 2009)	Minima reconstruction technique, MRT	2 CCD cameras			Burner	
Upton *et al.*	2011	Exp. Fluids (Upton *et al.*, 2011)	3D, computed tomography (CT)	6 cameras		0.25 mm	Burner	
Harker *et al.*	2012	Combust. Sci. Technol. (Harker *et al.*, 2011)	3D, Mie-scattering technique	Rotating mirror, 1 camera, thin multiple laser sheet	0.5 mJ	0.7 mm	Explosion flames	18 kHz
Kang *et al.*	2015	Proc. Combust. Inst. (Kang *et al.*, 2015)	FBEs, CH^* chemiluminescence	1 camera	No laser	0.1 × 0.1 × 0.2 mm	Burner	1 kHz
Wellander *et al.*	2011, 2014	OPTICS EXPRESS, Meas. Sci. Technol., Exp. Fluids (Wellander *et al.*, 2011; Wellander *et al.*, 2011; 2014)	OH-PLIF, Mie scattering	1–2 cameras			Dense spray, burner	1–2 kHz
Kristensson *et al.*	2011	Proc. Combust. Inst. (Kristensson *et al.*, 2011)	Mie scattering	1 camera		512 × 512 pixels in 6.2 × 6.2 mm^2	Dense spray	10 Hz

TABLE I. (*Continued.*)

Authors	Year	Journal, Ref	Measurement technique	Equipment	Laser pulse energy	Voxel size	Apparatus	Ext info
Meyer *et al.*	2016	OPTICS EXPRESS (Meyer *et al.*, 2016)	LII	8 cameras	1 J	0.13 mm^2/pixel	Jet flame	10 kHz
Ma *et al.*	2015	Appl. Phys. B Lasers and Optics (Ma *et al.*, 2015)	Tomographic chemiluminescence, TC, and fiber-based endoscope, FBE, CH* emission	2 cameras		0.5 mm voxel size	Supersonic combustor, ignition	20 kHz
Ma *et al.*	2017	Proc. Combust. Inst. (Ma *et al.*, 2017)	3D VLIF, CH radicals	Laser-sheet slab, 5 cameras	10 mJ	0.15 mm	Burner	10 Hz
Ma *et al.*	2017	Opt. Lett. (Ma *et al.*, 2017)	2D LIF, 3D VLIF, CH radical, tomography with LIF	6 cameras, laser sheet, laser slab	0.5 mJ for PLIF, 13 mJ for VLIF	0.041 mm for PLIF, 0.18 mm for VLIF	Hi-Pilot burner	10 Hz

mean reaction progress variable at 25 different planes to reconstruct the 3D flame, which was not instantaneous.

Kang *et al.* (2015) demonstrated the feasibility of instantaneous 3D flame measurements using fiber-based endoscopes (FBEs) to gather projections from various orientations simultaneously. They reported the practical advantages of FBEs for overcoming optical access and reducing equipment cost; however, these authors' technique was limited by signal attenuation due to the coupling and transmission losses in FBEs, leading to a degradation of the image quality. More recently, from the same research group, Ma *et al.* (2017) demonstrated the feasibility and accuracy of 3D turbulent flame diagnostics based on volumetric laser-induced fluorescence, VLIF. The technique required five cameras to simultaneously capture CH radicals in the flame to reconstruct 3D flame surfaces. Wellander *et al.* (2011; 2014) and Kristensson *et al.* (2011) used dual-mirror laser scanning technique with Mie scattering and OH planar laser-induced fluorescence, PLIF, for 3D reconstruction of dense sprays and low turbulence premixed flames, respectively. They reported the advantages and limitations of their technique with respect to spatial and temporal resolution. They also concluded that this technique with high-frequency lasers and high repetition rate cameras can be applied to highly turbulent flames.

Of pertinence to the present study, Harker *et al.* (2012) presented a study of turbulent premixed, lean methane–air flames developing in the Leeds fan-stirred combustion vessel, CV2, at low Karlovitz numbers, using a multiple laser-sheet imaging technique. An Oxford Lasers LS20-50 copper vapor laser, pulsed at a frequency of 18 kHz, was used to provide pulses of laser light, which were shaped into thin sheets using a number of lenses. The resulting laser sheets were swept through the CV by reflection off a rotating octagonal mirror. This allowed a number of "sweeps" through a flame during its development. However, due to the small sheet height of 50 mm and the finite time required within and between each sweep due to the low laser repetition rate, only flames developing at low turbulence and in the early stages of growth could be imaged. The resolution of 0.7 mm per pixel in all directions allowed structures of the integral and Taylor length scales of turbulence (20 and 3 mm, respectively) to be resolved, but not the Kolmogorov scale (0.15 mm).

Turbulent combustion is certainly a complex phenomenon and is still only partially understood. The third dimension of turbulent flames cannot be resolved by mere 2D flame imaging techniques. Therefore, it is necessary to analyze turbulent flames in 3D due to their inherent nature. Very limited 3D measurements have been carried so far, and there is need for accurate 3D measurement data of important structural parameters for turbulent flames (Driscoll, 2008; Hult *et al.*, 2007). Because of the rapid development of computational techniques such as large eddy simulation, LES, and direct numerical simulation, DNS, a number of 3D numerical studies (Dave *et al.*, 2018; Nivarti and Cant, 2017) have been carried out to investigate turbulent burning. However, there is lack of 3D experimental data to validate these studies. Both LES and DNS can only be applied to flows of low Reynolds numbers even with the state-of-the-art computing technology and thus with only lightly wrinkled flames. For the first time, the technique described in the present study is able to provide the required data for such validation studies.

Although 2D measurement techniques are designed to slice through the center plane of the flame, it is difficult to predict which part/plane of the flame has been captured as flame development is inherently 3D. This is particularly problematic for flames at high root mean square (RMS) turbulence intensity due to the developing flame convecting away from the point of ignition/imaging. The current swinging sheet technique allows the analysis of flames developing at high u' without the necessity of making assumptions about the relationship between 2D flame structure and the extension of this into the third dimension. The technique described by Harker *et al.* (2012) has been significantly developed in the present study. A Laser Lines Nd:YAG laser was employed to generate thin laser sheets at a height of approximately 100 mm in the center of the vessel. The use of a rotating mirror allowed a time interval between sweeps that successfully enabled a fully temporally resolved 3D study of turbulent explosion flame to obtain surface structure at engine-like turbulent conditions. The experimental data were processed using algorithms developed in the MATLAB programming environment to determine flame parameters such as total surface area, A, mean surface area, a, and reaction progress variable, $\bar{c}$. These were then compared with simulated data from DNS studies.

EXPERIMENTAL METHOD

Combustion vessel

The Leeds MKII fan-stirred combustion vessel is described in Lawes *et al.* (1998). It offers exceptional optical access by means of up to three pairs of orthogonally opposed fused silica windows of 100 mm thickness and is capable of withstanding starting mixture temperatures of up to 600 K and initial pressures of up to 1.5 MPa. Turbulence was created by four, eight-bladed orthogonally opposed 8 kW fans. The mean and RMS turbulent velocities, u', and integral length scale, L, were determined using laser Doppler velocimetry and particle image velocimetry (Bradley *et al.*, 1996). The turbulence was found to be uniform and isotropic (Nwagwe *et al.*, 2000) within the central 150 mm region of the vessel, with an L, of 20 mm and independent of the fan speed between 1000 and 10 000 rpm, except at 500 rpm where it was found to be 24 mm (Lawes *et al.*, 2012).

The RMS turbulence velocity, u', is given by the following relation as determined by (Bradley *et al.*, 2019):

$$u'\left(\frac{m}{s}\right) = \mathbf{0.00124}N_f\,(rpm), \tag{1}$$

where N_f is the fan speed. A single, 2 kW electric heating coil provided heating in the vessel.

Laser ignition system

During the course of the present experimental measurements, an adapted version of the laser ignition system presented in Bradley *et al.* (2004) was used in conjunction with the 3D swinging laser-sheet technique in order to avoid spark plug interference in both the turbulent flow field and flame images captured by the camera. Figure 1 shows the schematic top view of the laser ignition system employed in the present work. A New Wave solo 120 Nd:YAG laser, I_gL, at a wavelength of 532 nm capable of a maximum pulse repetition rate of 15 Hz was used for ignition. The laser beam from the ignition laser head was first expanded, using a 47 mm plano-concave lens of focal length (f) −50 mm on to a plano-convex lens of $f = 250$ mm and diameter of 145 mm. This effected an initial contraction of the beam, before passing through a second plano–convex lens, with $f = 450$ mm and diameter of 150 mm. This in turn focused the laser beam at the center of the vessel to a minimum waist diameter (d_f) creating the spark for explosions. By initially expanding the beam prior to contraction, a smaller beam waist was afforded as indicated by the following relation (Steen, 1998):

$$\mathrm{d_f} = \frac{4 \cdot \mathrm{f_L} \cdot \lambda \cdot \mathrm{M}^2}{\pi \cdot \mathrm{d_{bL}}}, \tag{2}$$

where f_L is the effective focal length of second plano–convex lens, d_{bL} is the laser beam diameter on the second plano–convex lens, λ is the wavelength of the laser light, and M^2 is the beam quality factor. Thus, the present laser ignition system also avoided any unwanted sparks either side of the point of focus due to rapid contraction of the beam. The spark diameters were measured in the range 2–4 mm.

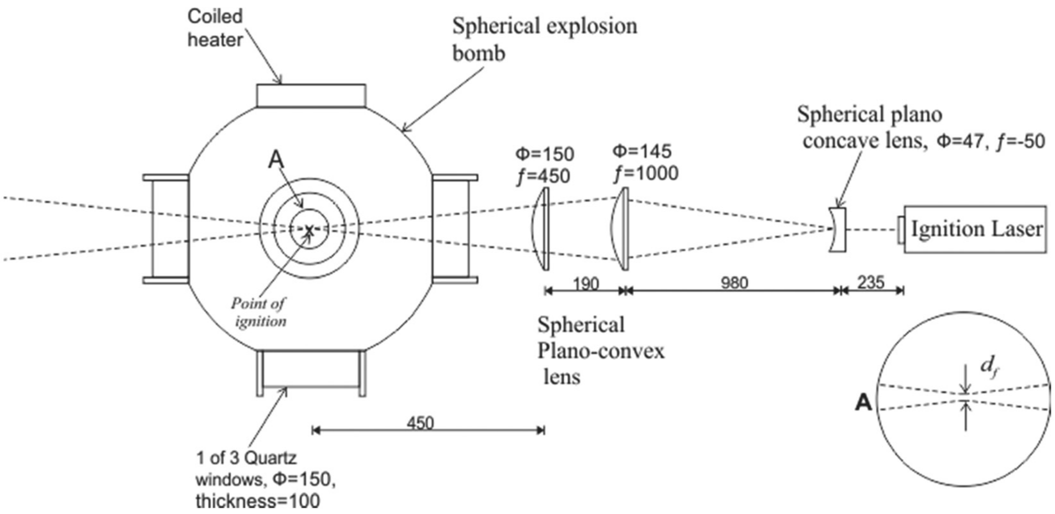

FIG. 1. Top view of a laser ignition set up, all dimensions are in mm.

3D swinging laser-sheet imaging technique

Schematic diagram of the 3D laser swinging sheet system is shown in Fig. 2.

Laser-sheet optics

Shown in Fig. 2 are the details of 3D laser swinging sheet system. A 532 nm Nd:YAG imaging laser, *IL*, with two internal cavities each capable of repetition rates ranging from 5 kHz to 30 kHz, provided the pulsed light source with a pulse energy of 13–1.9 mJ, respectively. Using dual cavity staggered pulsing, a maximum laser frequency of 60 kHz could be achieved at the minimum pulse energy. The beam from the *IL* head was first expanded through a plano–concave lens of $\Phi = 50.8$ mm with focal length, f, -100 mm, on to a plano–convex lens of $f = 250$ mm, and $\Phi = 50$ mm to focus at the center of the vessel in order to achieve a minimum sheet thickness, d_f of <0.6 mm, over a large focal distance. Using a pair of plano–convex cylindrical lenses with focal lengths $f = 38.1$ and $f = 25$ mm, respectively, before the 16-sided RM, a vertically expanded *IL* sheet approximately 100 mm in height was generated across the central area of the vessel. The RM was driven by an 8-pole synchronous hysteresis motor. The rotational frequency of the mirror was set using a control unit, supplied with the required frequency input by a Thurlby Thandar Instruments TGP 110 pulse generator. As the mirror motor was an eight-pole type, the input frequency to the motor drive unit was required to be eight times that of the desired motor shaft frequency.

As there was a finite time lag between the first flame image and the last flame image (1.44 ms) in one sweep of the *IL* sheet, it was important to select flames with sufficiently slow burning to minimise flame growth during the time of sweep. Consequently, only mixtures having a low laminar burning velocity, u_l, and at low turbulence levels, u', could be investigated. This still allowed flames with high Karlovitz stretch factors, K, to be investigated as the low value of u_l afforded high K values at relatively low u'. Increasing the RM speed would reduce the sweep time and the time between subsequent sweeps, however, at the cost of spatial resolution. Thus, a compromise was sought between the temporal and spatial resolution while minimizing the flame growth error during each sweep. Furthermore, details of the optical system for laser-sheet formation are presented in Ahmed (2019).

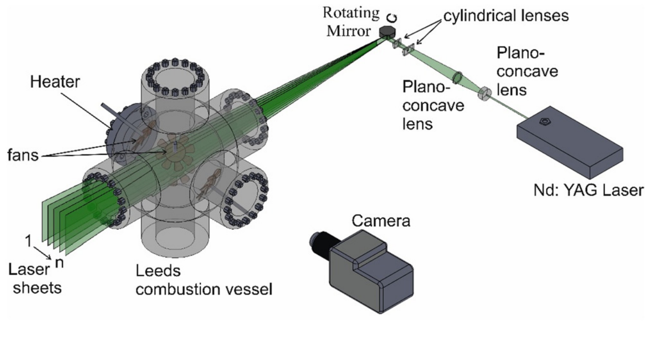

FIG. 2. Schematic diagram of the 3D laser swinging sheet system, laser ignition setup not shown.

Laser-sheet geometry

Depending on the rotational speed of the RM, there existed an angle between each sheet. Thus, for accurate reconstruction of the 2D images into a 3D reconstruction, it was necessary to take this into account. Shown in Fig. 3 are the details of the RM geometric offset and divergence of successive *IL* laser sheets. The *IL* sheet passing through the center of the CV makes an angle 0 and is designated as $i = 0$, where i is the number of the sheet from the center of the vessel. The angle between all the other sheets with respect to the center of the CV is given by the equation

$$\zeta_n = \frac{360 \cdot \omega}{f_{IL}} i, \tag{3}$$

where ζ_n is the angle made by the ith sheet with the centerline of the CV, ω is the angular rotating frequency of the RM in radians/s, and f_{IL} is the imaging laser frequency in Hz. In addition to *IL* sheet divergence, the point of reflection on the RM causes a geometric offset, a_i, of each *IL* sheet from the centerline of the CV as illustrated in Fig. 3. It shows RM at time t_0, and after a time $t_0 + \omega \cdot dt$, it rotates through an angle $\theta_m \cdot A_m$ is half the distance between RM parallel faces. X_m is the diagonal distance between the center of the mirror face before and after rotation by angle θ_m and is given by

$$X_m = A_m \tan \theta_m. \tag{4}$$

The geometric offset, a_i, is then calculated using the sine rule of a triangle given by

$$\frac{a_i}{\sin \theta_m} = \frac{X_m}{\sin(45 + \theta_m)}. \tag{5}$$

The time between two successive sheets is given by

$$t_{sIL} = \frac{1}{f_{IL}}. \tag{6}$$

The time between two sweeps is given by

$$t_s = \frac{1}{\omega \cdot n_f}, \tag{7}$$

where n_f is the number of faces on the RM. In the present study, at $\omega = 12$ Hz and $n_f = 16$, the time between two sweeps was 5.21 ms. However, the time for each sweep with *IL* pulsing was around 1.44 ms. When the RM rotated through an angle θ_m, the angle of incident, I_1, made by *IL* with RM, does not change, while the reflected ray R_1 shifts to R_2 and the normal shifts from N_1 to N_2. The new angle made by the I_1 with the new normal N_2 is thus

$$\theta_{N2} = \theta_{N1} - \theta_m. \tag{8}$$

The new angle of reflection, $R_{2,}$

$$\zeta = \theta_{N1} - [\theta_{N2} - \theta_m] = 2\theta_m. \tag{9}$$

Therefore, for a given angle of rotation of θ_m for RM, the angle turned by each laser sheet was $2\theta_m$. It is evident from this that increasing the rotation rate of the RM increases the angle between successive sheets, thus reducing the number of sheets in a sweep of fixed total angle. However, the reduced time for a sweep increased the maximum possible number of sweeps before the flame grew to such a size that it was

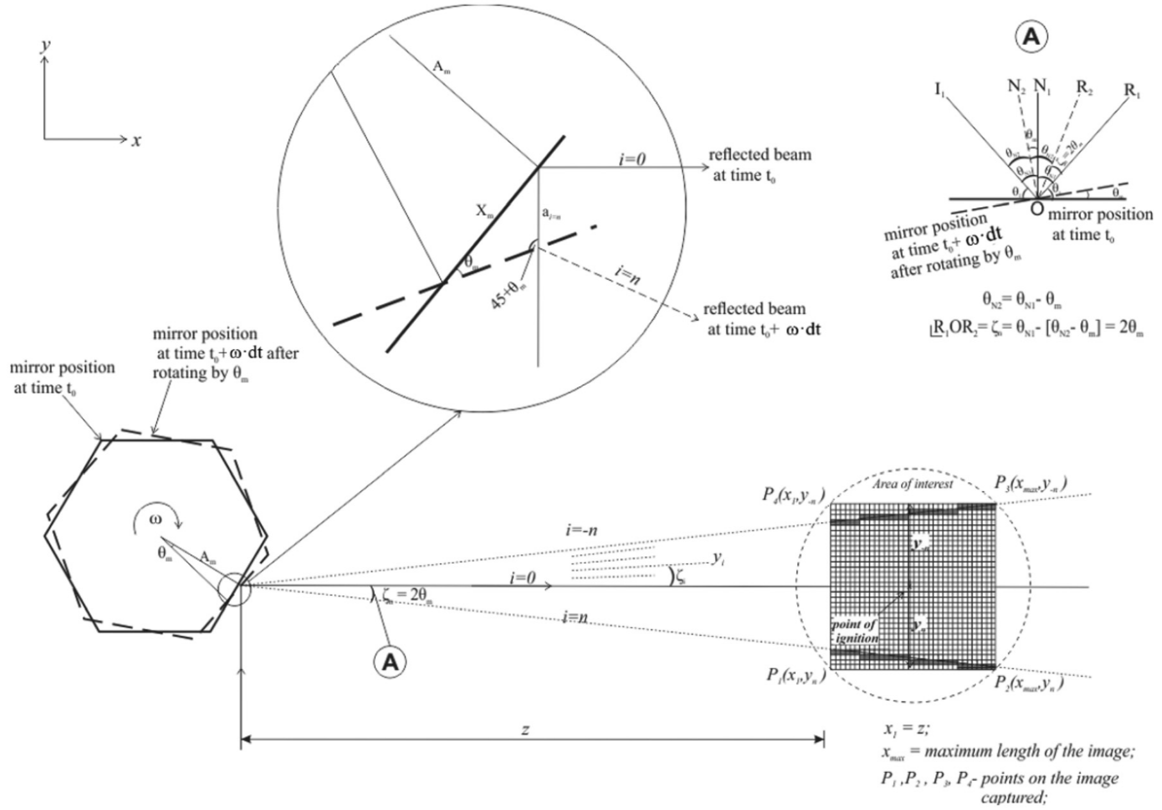

FIG. 3. Mirror geometric offset and divergence of successive laser sheets.

no longer contained within the field of view. For optimal image clarity, a maximum number of sheets per sweep was required. However, this would have limited the number of sweeps possible during flame growth. Thus, a compromise was sought between these factors in the present study.

Imaging system

Mie-scattered images were recorded using a high-speed phantom digital camera (VR2012) placed orthogonal to the *IL* sheets using a fixed Nikon macro objective lens of focal length 105 mm. The camera operated at a frame rate of 54 000 frames per second (*fps*), with an exposure time of 6 μs, at a resolution of 512 × 512 pixels, corresponding to 0.196 mm for the central sheet. The chosen exposure time (6 μs) yielded the best contrast between the burned gas (flame) and background. The *IL*, I_gL, *RM,* and camera were all synchronized to obtain fully time-resolved data of the flames. For the present work, *IL* and I_gL were pulsed at 54 kHz and 12 Hz, respectively. Typically, 78 sheets were recorded in each sweep of 1.44 ms duration and at a f_{IL} of 54 kHz.

As there existed a finite physical distance between the "first" and "last" sheets in each sweep with respect to the camera, a large depth of field, DOF, was used to strike the best compromise between individual sheet image clarity and the overall clarity of each sheet image in the sweep. A narrower DOF would have given very high image focus for several of the middle sheets in each sweep, but poor focus for others away from the center. A large DOF was not found to cause any significant problems with the subsequent processing of the images obtained. Nevertheless, the variation of pixel size, depending upon the position of the image, was considered while reconstructing the 3D flames. This was accounted for by measuring the pixel size at the three different positions in the CV. One was at the closest position to the camera, one at the center of the vessel, and the third at the farthest location from the camera. The pixel size was found to vary in a linear fashion with distance, and this was incorporated in the relevant calculations.

An olive oil droplet mixture in air was used as the seeding material, with a typical diameter of 1.06 μm and a density of 970 kg/m^3 (Melling, 1997). The partial pressure of the seeding mixture was kept to less than 4% of the total (fuel + air) mixture for the present case studied. Although a slight variation in the nominal equivalence ratio, Φ, is expected, experiments with up to 8% of seeding mixture showed no significant change in the turbulent burning rates.

DATA PROCESSING TECHNIQUE

Raw and binarized image data

Shown in Fig. 4(a) is a typical raw 2D Mie-scattered image acquired during the process for a CH$_4$/air explosion at $\phi = 0.7$, P = 0.1 MPa, T = 300 K, and at low turbulence of $u' = 0.3$ m/s. ($K = 0.027$). Laser light intensity was found to be highest in the center of the image than at the edges due to the inherently Gaussian nature of laser beam intensity. Due to low level of applied turbulence and thus

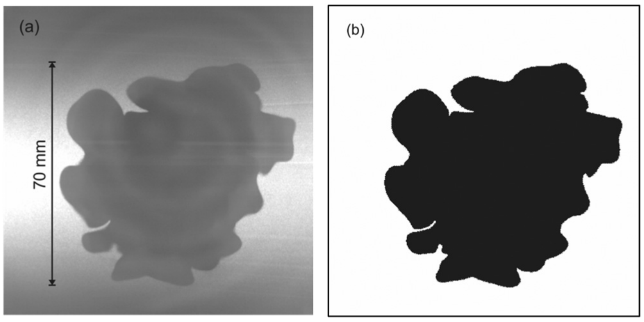

FIG. 4. (a) Raw Mie-scattered image. (b) Binarized image.

low value of K, the flame surface was mildly wrinkled, and as a result, the flame edge was clearly defined. The height and width of each image was approximately 100 mm.

These raw flame images were binarized, as shown in Fig. 4(b) before using them for 3D reconstruction. This was achieved using built-in filter functions in MATLAB such as the *log* (Laplacian of Gaussian) edge detection algorithm. The Laplacian filter detected the flame edge based on a user-defined gradient, while the Gaussian filter reduced the noise. This two-step process resulted in a good compromise by successfully detecting the flame edges and minimizing the spurious edge detection caused due to the intensity difference in the image background. Once the flame edge had been detected, the enclosed area in the binary image was filled using the built-in *imfill* function in MATLAB. Care was taken to ascertain that small flame surface details, particularly observed in high turbulence flames, were not accidentally removed. Finally, the *imcomplement* function was used to invert the pixel values, thereby leaving the final binarized image as shown in Fig. 4(b). This was necessary for the subsequent procedures.

3D flame reconstruction/assembly

After binarizing the 2D images following successful flame edge detection, the sheet images were assembled into a pre-allocated 3D matrix of 512 × 512 × 512 size volume elements (voxels) of initial value of unity, where the positions for insertion of the sheets into the matrix were calculated according to the angle between successive sheets θ_m and the geometric offset from the rotating mirror, a_g. These parameters were used to generate a straight line equation given by

$$y = \tan\zeta \cdot (Z + x) + a_g. \qquad (10)$$

Z is the distance between the *RM* and the first point on the plane of interest. Thus, for any x/y coordinate in the 2D image, the corresponding z coordinate in the third dimension was calculated. The process was then repeated for all the 2D sheets in a sweep to insert the values of 2D pixels in the corresponding coordinates in the 3D matrix. Because of the finite resolution in the array, the values of z coordinate were rounded off to the nearest integer. This resulted in a slightly stepped appearance of the inserted sheet as shown in the bottom right of the Fig. 3 (circled grid) where the stepped appearance has been exaggerated for clarity. The reconstructed volume size was approximately 100 × 100 × 104 mm^3. The resolution in the sweep direction was 0.74 mm.

Interpolation, surface mesh generation, and surface mesh smoothing

Figure 5(a) shows a cross section, through the Y-axis, of the assembled 2D sheets of a CH_4/air flame at $\phi = 0.7$, $P = 0.1$ MPa, $T = 300$ K and at low turbulence of $u' = 0.3$ m/s ($K = 0.027$) into a 3D matrix at 26.75 ms after ignition. It was necessary to interpolate between the sheets in order to generate a solid reconstruction and subsequent mesh generation of 3D flames. In the present study, the small spacing between successive sheets afforded the possibility of simply thickening the sheets slightly using the *imdilate* function. This function dilates the values based on the structuring neighborhood where typically single pixel/voxel spacing is present between the sheets. For cases with larger sheet spacing and/or higher values of K, a more complex, interpolative algorithm would have been required. The method employed here resulted in "solid" 3D flame structures, where an example of a cross section through the y-axis is shown in Fig. 5(b). This clearly shows that the filled image in Fig. 5(b) is a good representation of the original, unfilled version shown in Fig. 4(a).

Following this process, a triangulated surface mesh was generated using *isosurface* and *patch* functions in MATLAB. The *isosurface* command generated coordinates corresponding to user-defined isovalue positions, between 0 and 1, and in the present work, a value of 0.5 was used. Using the list of isovalue coordinates, the *patch* function

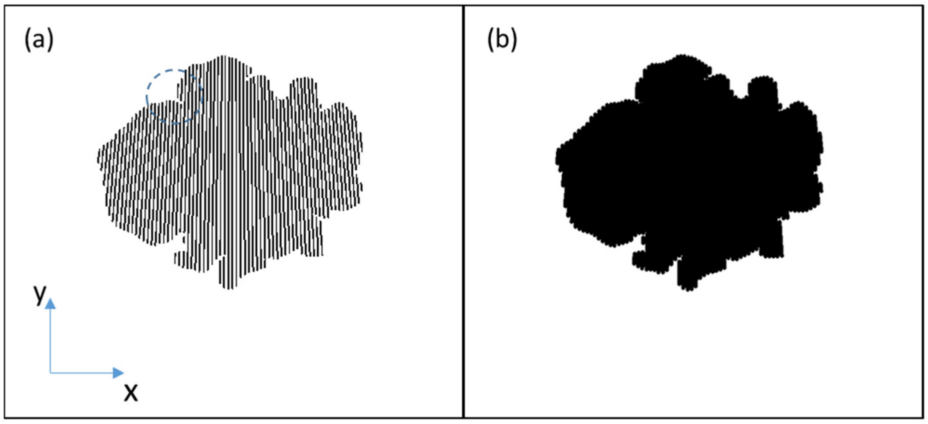

FIG. 5. A view of the cross section through Y-axis of (a) the assembled 2D sheets into 3D matrix with finite sheet spacing and (b) a solid 3D flame structure after interpolation.

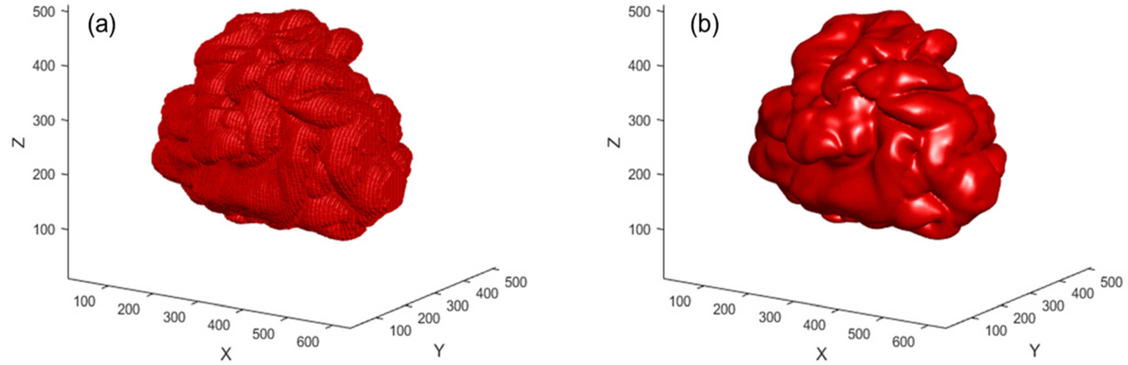

FIG. 6. CH_4/air at $\phi = 0.7$, 300 K, 0.1 MPa, $u' = 0.3$ m/s at t = 26.75 ms after ignition (a) unsmoothed and (b) smoothed.

generated a triangulated surface mesh, linked by vertices at the coordinates returned by the *isosurface* function. Figure 6(a) shows an example of the resulting surface mesh structure. The stepped and flat surfaces, which are not a good representation of the flame with a concomitant high surface area, were eliminated in Meshlab using a smoothing algorithm described in Taubin (1995), which minimized shrinkage by incorporating an expansion term and retained the surface features (such as flame curvatures) and volume of the reconstructed flame. This algorithm operated by moving the vertices of the triangulated surface without altering the connectivity of the faces. Therefore, the operated surface contains exactly the same number of vertices and faces as the original surface. Shown in Fig. 6 is an example of the unsmoothed and smoothed flame reconstruction at $u' = 0.3$ m/s for CH_4/air flame. Flat faces and steps can be seen in the unsmoothed reconstruction, Fig. 6(a), while the smoothed version, Fig. 6(b), displays none of these leaving the surface features such as flame wrinkles intact representing more closely the actual flame. Nevertheless, smoothing reduced the total flame surface area by 25% for the largest and highly turbulent reconstructed flame. Furthermore, details on interpolation, surface mesh generation, and smoothing are presented in (Thorne, 2017).

3D RECONSTRUCTED FLAME PARAMETER ANALYSIS

Various flame parameters such as total flame surface area, A, mean flame surface area, a_v (based on balancing of burned and unburned volume), and a_m (based on balancing of burned and unburned masses), flame volume, and reaction progress variable, $\bar{c}$, were obtained from the smoothed 3D reconstructions and evaluated.

Total flame surface area/wrinkled flame area, *A*

The total surface area, A, of the triangulated flame surface mesh was now found by calculating the area of each triangle in the flame mesh, using the cross product of the two vectors, which represent the sides of each triangle and subsequently summing the areas of all triangles constituting the surface mesh. If $\vec{a}$, $\vec{b}$ represent the vectors of a triangle, then the magnitude of the cross product of these two vectors, as sides of the parallelogram, gives the area of the parallelogram made by them. The area of the triangle formed by these vectors is then given by

$$A_I = \frac{1}{2}|\vec{a} \times \vec{b}|. \tag{11}$$

Now, the total sum of areas of all the triangles gives the total surface area, A, of the turbulent flame as

$$A = \sum A_I. \tag{12}$$

Mean flame area, *a*

The triangulated surface meshes were converted into solid reconstructions consisting of voxels representing burned gas using the "polygon2voxel" algorithm presented by Kroon (2016). By calculating the volume of each voxel, an estimation of the entire volume of each 3D reconstruction was obtained.

The mean surface area, a, was calculated based on volume balancing, a_v, and also on mass balancing, a_m, of unburned and burned gases. Figure 7 shows two different views of the same turbulent flame for CH_4/air at $u' = 0.3$ m/s and $\phi = 0.7$, 300 K, 0.1 MPa. It shows the distribution of burned and unburned gas at t = 26.75 ms after ignition. R_r and R_t represent the root and tip radius of spheres drawn from the centroid of the flame to $\bar{c} = 0$ and $\bar{c} = 1$, respectively. A general radius R_j lies in between these two radii within which and outside R_r, m_{ui}, and V_{ui} are the total mass and total volume of unburned gas and m_{bi} and V_{bi} are the total mass and total volume of burned gas, respectively. Outside R_j and within in R_t, m_{uo}, and V_{uo} are the total mass and total volume of unburned gas and m_{bo} and V_{bo} are the total mass and total volume of burned gas, respectively. To calculate the mean area a_v based on volume balancing, R_j was found such that the total volume of

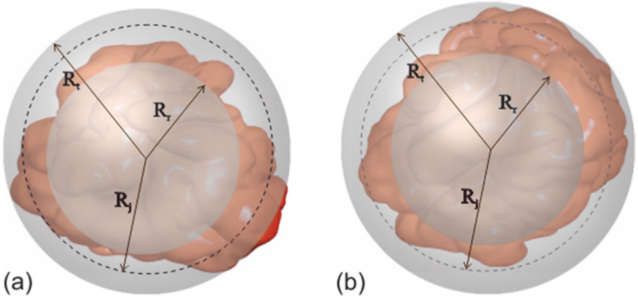

FIG. 7. Two different views of the same CH_4/air at u'=0.3 m/s and $\phi = 0.7$, 300 K, 0.1 MPa.

unburned gas, V_{ui}, inside it is equal to the total volume of burned gas, V_{bo}, outside it. Similarly, to calculate the mean area a_m based on mass balancing, R_j was chosen such that the total mass of unburned gas, m_{ui}, inside it is equal to the total mass of burned gas, m_{bo}, outside it. The two different views demonstrate how R_t could be miscalculated from 2D imaging as Fig. 7(a) shows the sphere R_t slicing through the flame while in fact it is passing through the farthest flame edge when viewed through a different angle as shown in Fig. 7(b). Once the centroid of all of the burned gas was found, starting from $R_j = R_r$ until $R_j = R_t$, the respective unburned and burned gas volumes outside and inside were calculated and plotted against mean radius, varying between R_t and R_r, an example of which is shown in Fig. 8(a). The point at which the unburned and the burned gas volumes intersect is taken as the mean $R_j = r_v$, using which a_v is calculated from Eq. (4). Similarly, the respective unburned and burned gas masses outside and inside R_j were calculated and plotted against mean radius varying between R_t and R_r, an example of which is shown in Fig. 8(b). The point at which the unburned and the burned gas masses intersect was taken as the mean radius, $R_j = r_m$, using which a_m is again calculated from Eq. (5).

Burned gas volume

The mean radius, a_v, was also found from the volume, V, of the flame. Here, V was calculated by summing the volumes of all the voxels, which constituted the burned gas. The volume, v_i, of each voxel is determined based on camera resolution and, in the present case, is 0.0075 mm^3 and is thus known. Therefore, the total volume of the flame is calculated using the equation below:

$$V = \sum n \cdot v_i, \tag{13}$$

where n is the number of burned (black) voxels with a value of zero. This volume, V, may be equated to the volume of a sphere using Eq. (4), and hence, r_v can be derived

$$\boldsymbol{V = \frac{4}{3}\pi r_v^3}. \tag{14}$$

Using r_v, the mean surface area a_v may be calculated as

$$a_v = 4\pi r_v^2. \tag{15}$$

The surface area ratio of the 3D reconstructed flame is then given by $\frac{A}{a_v}$. Similarly, values of a_m and the corresponding $\frac{A}{a_m}$ could also be found.

Reaction progress variable ($\bar{c}$)

Each Cartesian coordinate was converted to polar coordinates using the built-in 3D cart2pol function in MATLAB. Between R_r and R_t, successive shells of user-defined size were created starting from R_r, until R_t, and the number of burned and unburned voxels in every successive shell was determined. At each point, with the polar coordinates known, the fraction of burned voxels out of the total number of burned and unburned voxels combined at each of the radii between R_r and R_t yielded $\bar{c}$, where $\bar{c}$ at any given R_j is given by the equation

$$\bar{c}_{Rj} = \frac{n_b}{n_b + n_u}, \tag{16}$$

where n_b is the number of "burned" voxels and n_u is the number of "unburned" voxels. The full version of the scripts developed to post-process the current data and the associated MATLAB functions are presented in the Appendix of Ahmed (2019).

RESULTS

Experiments were conducted using a CH_4/air mixture at an initial temperature and pressure of 365 K and 0.5 MPa, respectively, at equivalence ratio, $\phi = 1.35$. This mixture was chosen due to its low u_l value of 0.095 m/s. For all experiments conducted, the residual gases were kept as low as 0.06%. The burned gas density, ρ_b, unburned gas density, ρ_u, kinematic viscosity, ϑ, of the mixture were 0.746, 4.492 kg/m^{3,} and 4.6×10^{-6} m^2/s, respectively, as calculated using Gaseq (Morley,

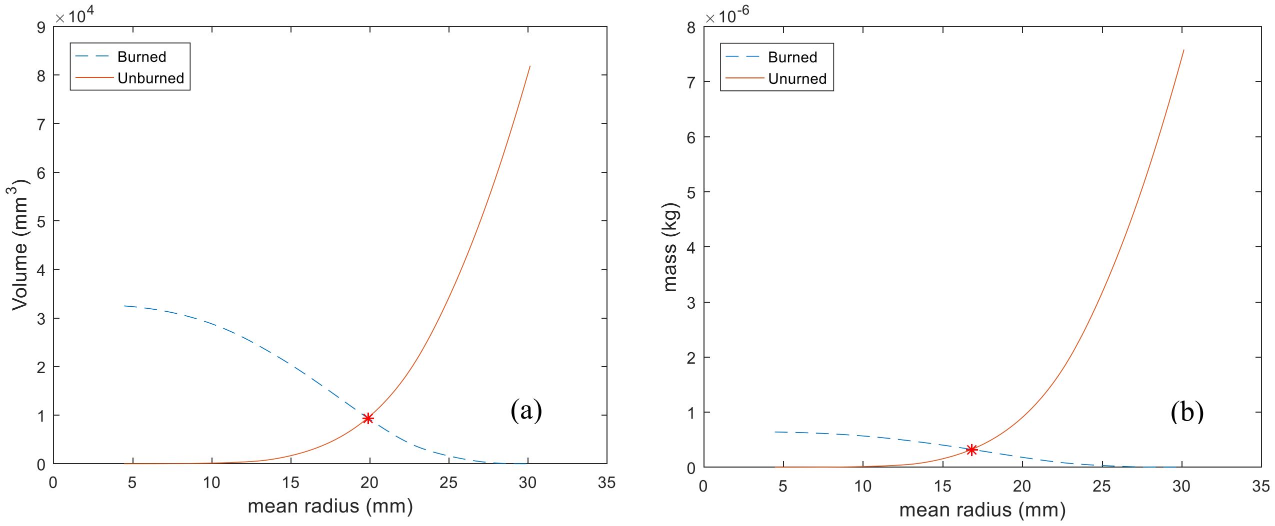

FIG. 8. Burned and unburned gas (a) volume (b) mass, across $\boldsymbol{R_j}$ for increasing mean radius for the flame shown in Fig. 7. Symbol * represents the point of burned/unburned gas equality.

TABLE II. Experimental conditions for the present study, units for the parameters: $\mathbf{T}\ (\mathbf{K})$, $\mathbf{P}\ (\mathbf{MPa})$, $\boldsymbol{u_l}\ (\mathbf{m/s})$, $\boldsymbol{\delta_l}\ (\boldsymbol{m}) = \frac{\vartheta}{u_l}$, $\boldsymbol{u'}\ (\mathbf{m/s})$.

	ϕ	T	P	u_l	Ma_{sr}	δ_l	u'	$R_L^{-0.5}$	u'/u_l	K
CH_4	1.35	365	0.5	0.095	6	4.84×10^{-5}	0.3	0.0277	3.158	0.069
							0.5	0.0214	5.263	0.149
							0.75	0.0175	7.895	0.273
							1.0	0.0152	10.526	0.420
							1.25	0.0136	13.158	0.587
							1.5	0.0124	15.79	0.772

2005). To study the effects of increasing rms turbulence velocity, u', on turbulent flame structure, discrete u' values ranging from 0.3 m/s to 1.5 m/s were employed, see Table II. This led to Karlovitz stretch factor, K, values varying from between 0.046 and 0.79.

Shown in Fig. 9 are a set of 2D flame images obtained during a sweep at 16.3 ms after ignition. A total of 60 slices of a 3D flame were captured at this instant out of which every fourth raw image is shown. The resolution of each image, 512 × 512 pixels, was equivalent to 100.35 × 100.35 mm at the center of the combustion vessel. The sheet separation distance in the third dimension was approximately 0.5–0.6 mm. Looking at these individual images, it is difficult to predict the overall shape of the flame and also its 3D surface structure. When the

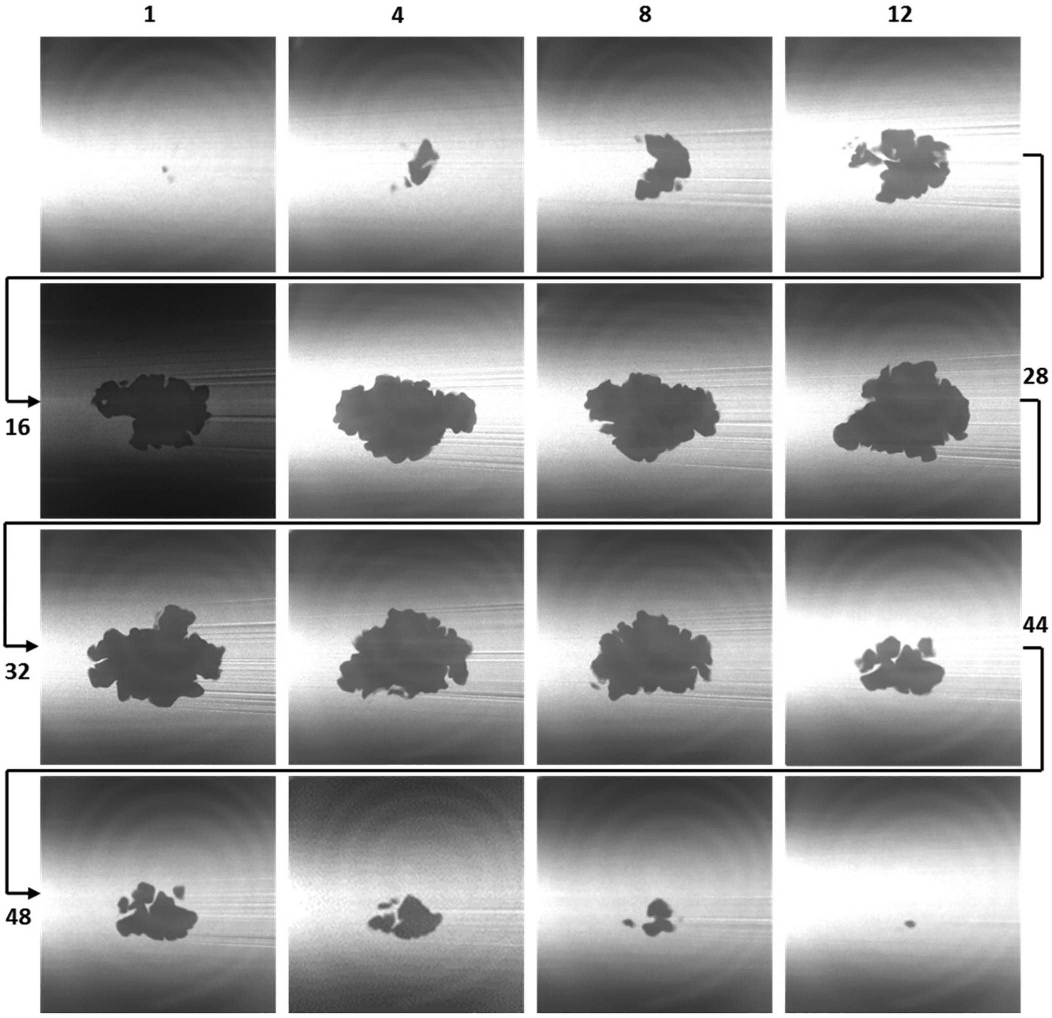

FIG. 9. Set of raw flame image data in one sweep at one instant. $u' = 0.3$ m/s and 16.3 ms after ignition.

same flame is analyzed/imaged using Schlieren photography technique, this flame would appear almost spherical; however, the present technique reveals a considerable structure. Apparently, frame 48 has an island of flame detached from the main flame giving an appearance of two separate flames; however, these are in fact found to be interconnected with the main flame from frame 44. Thus, a 2D analysis with a fixed sheet position would have incorrectly implied that the flame existed in multiple, fragmented parts. In addition, frame 16 reveals a pocket of unburned mixture within the main flame further complicating the study. Again, analysis of this single sheet would imply that this region is isolated. However, analyzing the frames either side of this flame image shows that this region is clearly part of a deep wrinkle in the flame surface. In flames particularly at low turbulence, these apparent islands and pockets are in fact fingers of burned and unburned mixture interconnected to other gas regions on different planes (Gillespie *et al.*, 2000; Hicks *et al.*, 1994; and Mantzaras *et al.*, 1988). Furthermore, it is important as to which slice of the flame is considered for flame analysis while using 2D techniques as this would increase the uncertainty, if the slice captured do not go through the center of the flame. In particular, flames close to quench regimes of K tend to move from the center of the vessel, thereby increasing the uncertainty of slicing the flame through the center.

Figure 10 shows successive 3D reconstructions of a single CH_4/air flame with increasing time from ignition at $u' = 0.3$ m/s. The image at 16.3 ms represents the reconstructed 3D flame using the 2D images presented in Fig. 9. With increasing time from ignition, the flame radius as well as flame surface wrinkling increased due to increasing turbulent length scales. In the early stages of flame growth, the larger length scales merely convect the flame (Abdel-Gayed *et al.*, 1987). At low turbulence of $u' = 0.3$ m/s, as the flame grew, it retained its general shape formed during the ignition event while the surface became more wrinkled.

The flame shown in Fig. 11 at a higher value of $u' = 1.5$ m/s did not maintain its initial shape as it grew, with the surface being visibly highly wrinkled. The reconstructions shown exhibit very highly wrinkled surfaces in the later stages of growth, which increased the area ratio, A/a. However, higher u' values led to flames rapidly extending beyond the field of view, limiting the possible number of sweeps.

Any definition of turbulent burning velocity requires the associated radii and flame surface area to be characterized (Bradley *et al.*, 2011). Figure 12 shows the experimentally measured mean radii, r_v and r_m, against time, respectively, for increasing values of u'. The two different radii enable the associated burning velocity to be found. The symbols show the average of three explosions at the same condition and the error bar shows the variability. Solid/dashed lines are the best-fit curves through the measured data. Flame radii increased with time as well as u'. Even at identical initial conditions and near isotropic turbulence, the flames were quite different in shape/structure and the variance in the average flame diameter was of approximately 9% at lower flame radius and up to 26% at higher flame radius. This gives a rough measure of experimental variability in the very well controlled turbulent environment of the Leeds MKII fan-stirred combustion vessel.

Shown in Fig. 13 is a comparison of r_v and r_m values at different instances of flame development for u' of 0.3 and 1.5 m/s. Symbols are the measured data and solid/dashed lines are the best-fit curves through them. It has been shown in (Bradley *et al.*, 2003) that r_v can be more conveniently obtained from schlieren measurements, without the need for complex laser techniques, while r_m is associated with mass rate of burning and can be estimated from pressure measurements. It is observed that, within the measured field of view, the values of r_m are always lower than r_v. The difference increases with increase in time from ignition. The maximum difference observed was 13%.

As discussed in the previous section 'Experimental Method', each sweep through a developing flame takes a finite period of time of 1.44 ms. Thus, the flames grew slightly during image capture. The mean flame radius during each sweep grew approximately linearly with time; therefore, the error in its estimation is proportional to the sweep interval. With $u_l = 0.095$ m/s, $Ma_{sr} = 6$, at max $u' = 1.5$ m/s, and for the largest 3D reconstructed CH_4/air flame, the mean flame radius during the sweep, increased up to 14%. This is within the variance (see Fig. 12) of the reconstructed flames. Increasing the mirror rotation rate would have reduced the time between sweeps, with a concomitant reduction in 3D spatial resolution. The use of high-imaging laser repetition rates allows good spatial resolution, while increase in the RM facets with increased frequency would minimize intra-sweep times simultaneously. However, the number of facets is limited by the sweep area that is required to give a sufficiently broad sweep through the region of interest.

Flame area ratio, A/a

Shown in Fig. 14 are the A/a_v and A/a_m values obtained for developing flames against increasing radii r_v and r_m, respectively, for increasing values of u'. Values of A were found using Eqs. (11) and (12) as described in the method section. Values of a_v and a_m were obtained using Eq. (14) using r_v and r_m, respectively. The symbols represent the average of three identical explosions, and the error bar shows the variability. The solid lines are the best-fit curves through these data. It is observed that both A/a_v and A/a_m increase with increasing radius as well as u'. The surface area ratio increased with radius, due to the range of turbulence length scales to which the flame was exposed. This corresponds to an increase in the effective RMS turbulent velocity, u'_k (Abdel-Gayed *et al.*, 1987). Higher u' values typically lead to a sharper rise in *A*/*a*. Some of the *A*/*a* values are relatively high immediately after ignition, where distortion of the flame shape due to laser ignition is likely responsible. Moreover, it was found that the values of A/a_v were lower than A/a_m.

Reaction progress variable, $\bar{c}$

Shown in Fig. 18 is the reaction progress variable, $\bar{c}$, plotted against radius from the flame centroid at 11.12 ms after ignition. This figure shows the variability in $\bar{c}$ for three identical explosions of the CH_4/air mixture at $u' = 0.3$ m/s. The curve progresses asymptotically to a value of unity, representing fully burned gas, at smaller radii toward larger radii with a value of zero, representing unburned gas. Values of radius at $\bar{c} = 1$ and the maximum radius at $\bar{c} > 0$ give r_r and r_t, respectively. It also shows the turbulent flame brush thickness, δ_t, measured between $\bar{c} = 0.1$ and 0.9. The average radius for the data presented in Fig. 15 is 16.5 mm, while the horizontal bar showing the variability measures approximately 5 mm.

Figure 16 presents the mean variation of $\bar{c}$ with flame radius at different instances in time during an explosion under $u' = 0.3$ and 1.5 m/s, respectively. The horizontal bar shows the variance from three explosions. The variable r_r was found to vary little while r_t changed

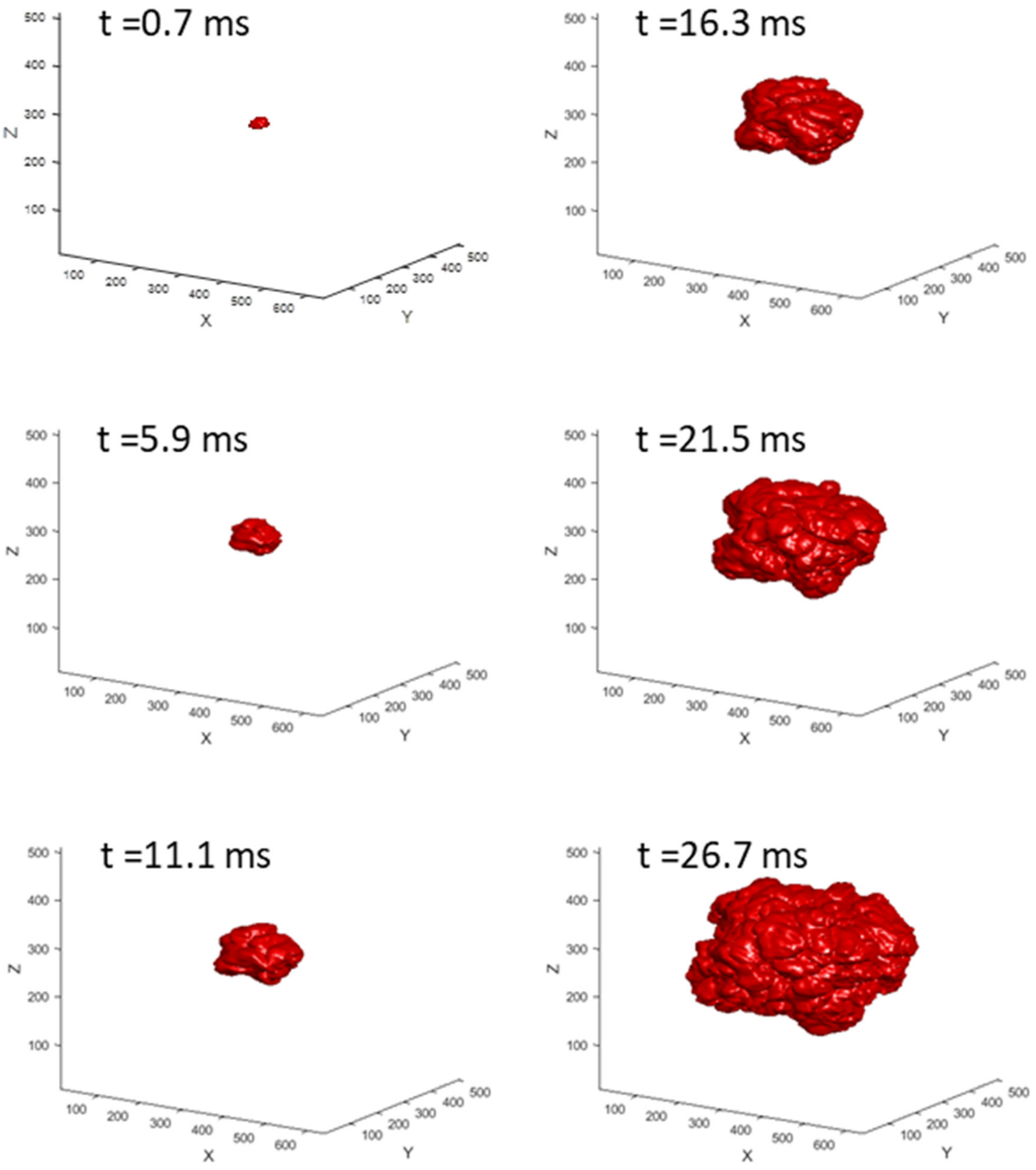

FIG. 10. 3D reconstructed CH_4/air flames with increasing time during an explosion at $u' = 0.3$ m/s.

dramatically with increasing time after ignition. The gradients of these curves are found to decrease with increasing time as the flame develops indicating an increase in δ_t. It is interesting to note that the gradient in $\bar{c}$ for the curve in Fig. 16(a) at 21.5 ms is similar in magnitude to that of the curve in Fig. 16(b) after 11.1 ms. This shows that the flames in Fig. 16(a) were considerably slower growing than those analyzed in Fig. 16(b).

Shown in Fig. 17 is the turbulent flame brush thickness, δ_t, with increasing time at three different u' values. As the flame grew, δ_t was found to increase with both time and u'. This demonstrates that the flame became increasingly wrinkled as it grew. This is because of the increase in flame size, which leaves more surface area for the turbulence to act on, leading to an increase in wrinkling. This explains the rapid increase in δ_t at high u' due to faster flame development.

Mean flame radius at a $\bar{c} = 0.5$, $r_{\bar{c}=0.5}$, a particularly useful representative flame radius described by Bradley *et al.* (2003), was also obtained and are compared with the mean radius based on volume balancing, r_v, in Fig. 18. This figure shows the comparison of r_v and

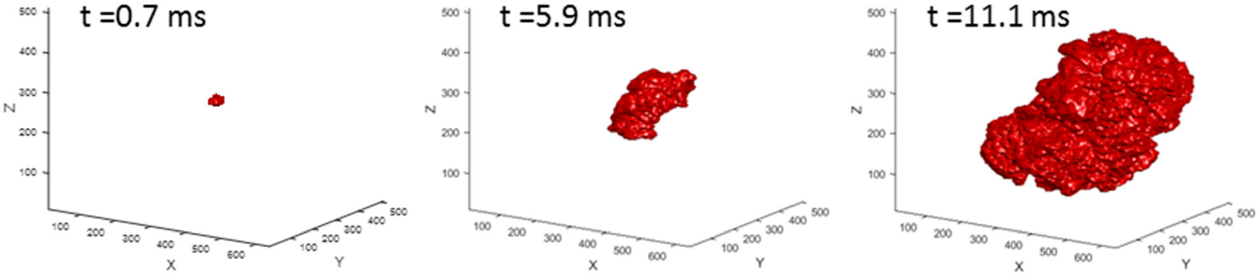

FIG. 11. 3D reconstructed CH_4/air flames with increasing time during an explosion at $u' = 1.5$ m/s.

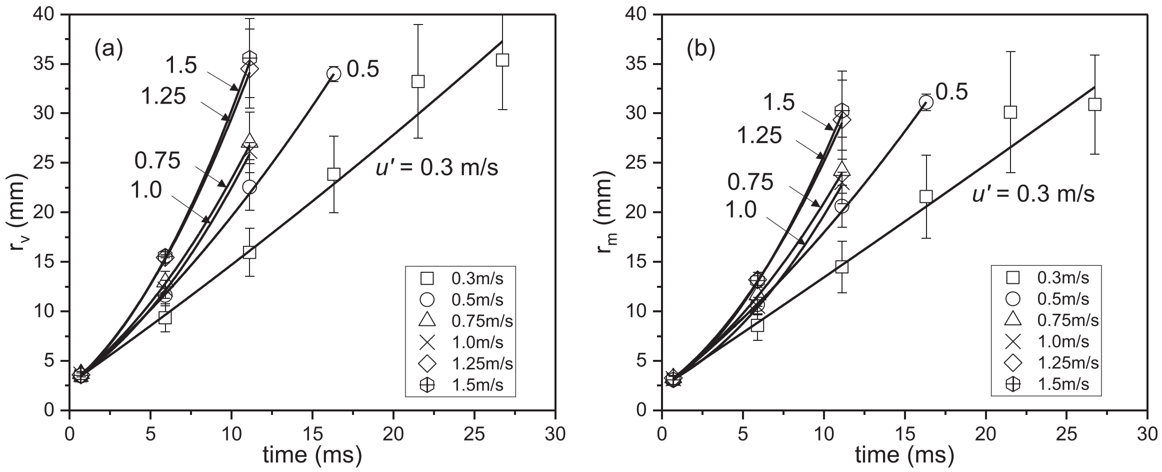

FIG. 12. (a) r_v against time and (b) r_m against time for increasing values of u'.

$r_{\bar{c}=0.5}$ for three different u' values with increasing time. The symbols show the average of three explosions at the same condition. Open symbols represent r_v, and filled-in symbols represent $r_{\bar{c}=0.5}$. No significant difference was observed between the two. The data presented in Fig. 18 can also be used to calculate turbulent flame speed, S_t, by calculating the slope of the linear fit (not used in Fig. 18) through the data; however, this was not the objective of the current study, and therefore, these were not explored in detail.

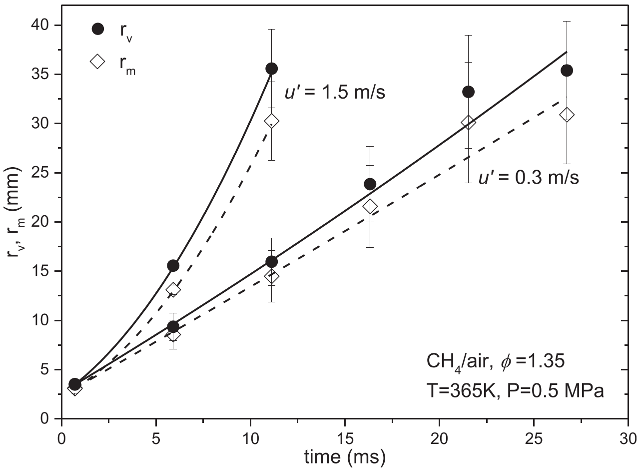

FIG. 13. Comparison of r_v and r_m against time for $u' = 0.3$ and 1.5 m/s.

DISCUSSION

In the present study, flame surface areas and reaction progress variable were measured directly, without the need for the assumptions made when analyzing fixed laser-sheet position-derived 2D images. The effect of sheet spacing on flame reconstruction was explored, and it was found that reducing the sheet spacing reduces the flame surface area (Thorne, 2017). From the present data, it has been calculated based on linear behavior that the surface area of a theoretical reconstruction with zero spacing would be 3.8% lower than that for the actual case with a single pixel spacing. The effect of the sheet spacing employed here is thus small. However, the reconstruction revealed that removing the intermediate sheets leads to the generation of large flat edges, which increases surface area.

To obtain generality, Fig. 19 shows a comparison between A/a_v and A/a_m values for increasing values of u'/u_l. Filled symbols and solid lines are the experimental results and best-fit curves through the data presented while open symbols and broken line show the DNS data and the best fit through it DNS (Nivarti and Cant, 2017). These

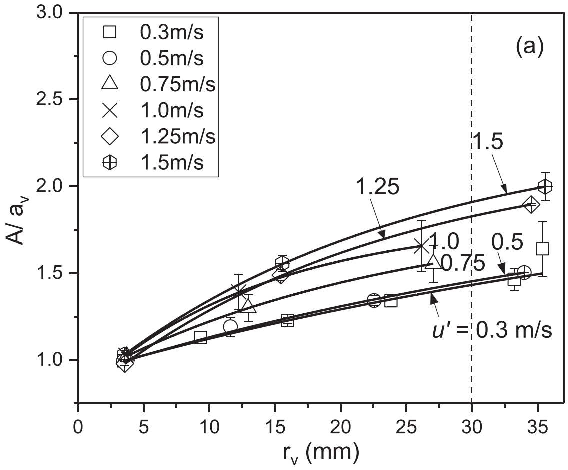

FIG. 14. (a) A/a_v against r_v and (b) A/a_m against r_m for increasing values of u'.

were compared at a flame radius of 30 mm where the $\frac{u'_k}{u'}$ value was found to be 0.7.

This value was chosen as it was only slightly greater than the maximum value typical of the largest reconstructions (thereby minimizing the amount of extrapolation required) and was the minimum value at which the flame experiences 70% of the turbulence. In cases such as at $u' = 0.75$ and 1.0 m/s where the maximum obtained mean flame radii fell short of 30 mm, as shown in Fig. 14, the A/a_v and A/a_m values were obtained by slightly extrapolating the trends. Again, the values of A/a_v are lower than A/a_m. Moreover, the discrepancy between the two increases with increasing values of u'/u_l. The maximum difference between the two was found to be approximately 28%

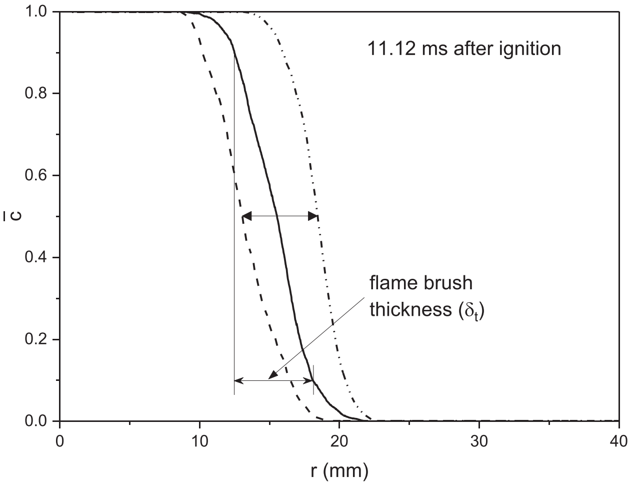

FIG. 15. Variation of $\bar{c}$ against radius for flame at 11.12 ms after ignition for three identical explosions of CH$_4$/air mixture at $u' = 0.3$ m/s. Turbulent flame thickness (δ_t) measured between $\bar{c} = 0.1$ and 0.9.

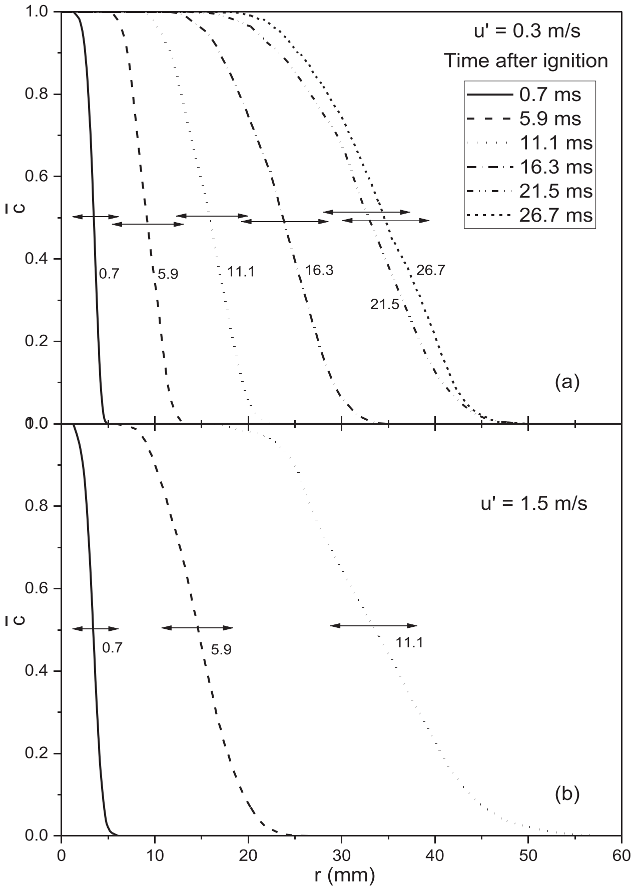

FIG. 16. Variation of $\bar{c}$ against radius with increasing time during CH$_4$/air explosion (a) $u' = 0.3$ m/s and (b) $u' = 1.5$ m/s.

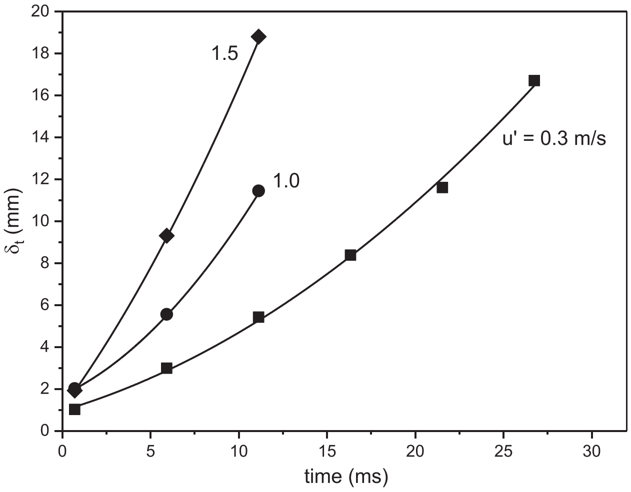

FIG. 17. Variation of turbulent flame thickness, δ_t, with increasing time at three different u' values.

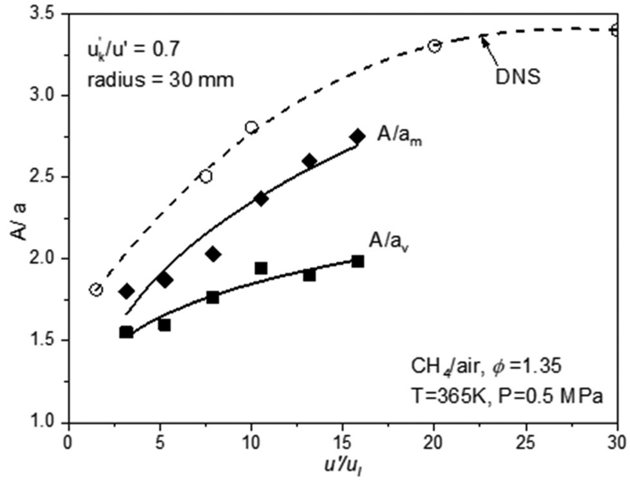

FIG. 19. Comparison of A/a_v and A/a_m values for increasing values of K.

at the highest K values reported in Fig. 19. The figure also shows the A/a ratios obtained from DNS (Nivarti and Cant, 2017). The present results are in close proximity with the results from DNS; however, a difference of 13% was observed between the present experimental results of A/a_m and the A/a obtained from DNS. This could be attributed to the different initial conditions employed for the DNS work.

Since $\bar{c}$ is a dimensionless parameter, it is logical to present it against a dimensionless number. Therefore, $\bar{c}$ is plotted against normalized radius in Fig. 20 at $u' = 0.3\,\mathrm{m/s}$. This demonstrates a better generalization, and interestingly, the gradient of $\bar{c}$ against $r/r_{\bar{c}=0.5}$ appears to be at a maximum, close to $\bar{c} = 0.5$. Similarly, generalities of $\bar{c}$ in terms of $r/r_{\bar{c}=0.5}$ for other u' are also sought.

Shown in Fig. 21 is a plot of $\bar{c}$ against normalized radius for increasing u' at 11.1 ms after ignition. The gradients of the curves are found to increase with increasing u' indicating an increase in δ_t.

The spatial resolution of the present swinging sheet technique is comparable to that of the VLIF techniques reported recently in Ma et al. (2017) and requires only one camera compared to five cameras for the latter with obvious savings afforded in experimental costs. Important flame parameters such as $\sum$ and flame curvatures can also be determined from these 3D reconstructions. However, these were beyond the scope of the present study. Finally, it is worth mentioning that the technique applied in this paper is not necessarily restricted to flame studies: it can be used for any 3D flow visualization purpose.

Limited by the camera resolution at high framing rates, the areas at Kolmogorov length scales, i.e., less than 0.19 mm in the current vessel could not be evaluated. Therefore, it was not possible to report the uncertainty in calculating the A/a at smaller length scales. Simultaneous Mie-scattering and OH-PLIF imaging for flame edge and reaction zone interrogation could shed more light on whether the edge detected by the Mie-scattering technique follows the reaction zone or if there is any

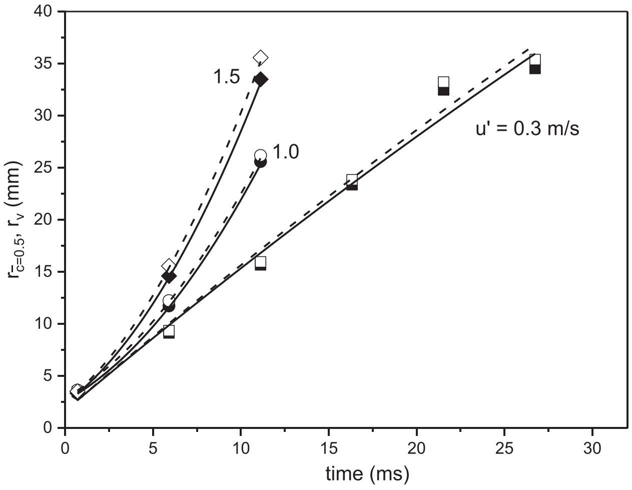

FIG. 18. Comparison of r_v and $r_{\bar{c}=0.5}$ with increasing time for three different u' values, open symbols, r_v, and closed symbols, $r_{\bar{c}=0.5}$.

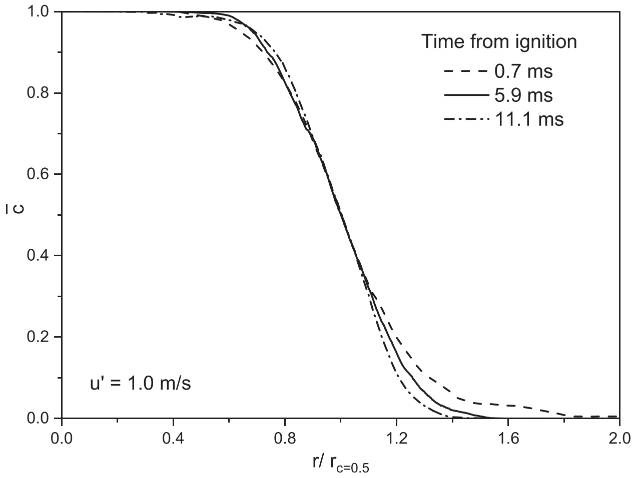

FIG. 20. $\bar{c}$ against normalized radius $r/r_{\bar{c}=0.5}$ for increasing after ignition for at $u' = 1.0\,\mathrm{m/s}$.

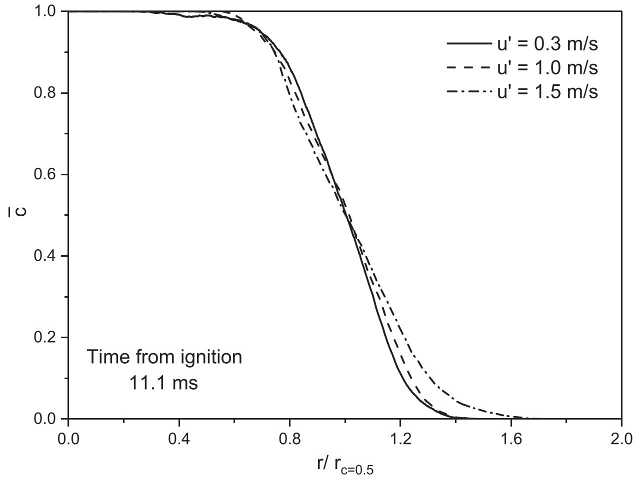

FIG. 21. $\bar{c}$ against normalized radius $r/r_{\bar{c}=0.5}$ at 11.0 ms after ignition for different $u\prime$ values.

flame area left undetermined. Increasing the working frequency limits of the camera, coupled with higher laser repetition rates, will aid in capturing flames with faster burning rates and also at high turbulence levels, which are relevant in many engine applications.

CONCLUSIONS

The present work describes the development of a multiple laser-sheet, Mie-scattered imaging technique for the study of flames developing at high Karlovitz stretch factor values. For the first time, this has allowed the direct measurement of wrinkled flame surface areas and mean flame surface area ratios without the need for the assumptions normally made when analyzing fixed plane, single laser-sheet images. This also provides data for direct comparison with simulation studies (e.g., DNS), where suitable data were not previously available for validation purposes. Algorithms were developed to reconstruct the 3D flame surface from 2D sheet images and determine various flame parameters such as total surface area, A, mean surface area, a, reaction progress variable, $\bar{c}$, and flame brush thickness. This 3D representation of the flame data provides more insight into the dynamic nature of the flame front topology such as turbulence and chemical reaction interaction. It also allows a more accurate representation of 3D flame structure, where seemingly separated areas of flames observed in 2D images can be seen in the present study to be connected to other parts of the flame. Furthermore, improvements in laser and camera technology could allow the technique to extend down to the Kolmogorov scale of turbulence and for a wider variety of fuels with faster laminar and turbulent burning rates.

ACKNOWLEDGMENTS

The authors would like to thank the EPSRC (Grant No. EP/W002299/1) and Shell Global Solutions for funding this work, and Brian Leach for technical support. The insights provided by Dr. Malcolm Lawes are greatly acknowledged.

AUTHOR DECLARATIONS

Conflict of Interest

The authors have no conflicts to disclose.

Author Contributions

Pervez Ahmed: Data curation (equal); Formal analysis (equal); Investigation (equal); Methodology (equal); Software (equal); Validation (equal); Visualization (equal); Writing – original draft (equal). **Benjamin John Alexander Thorne:** Conceptualization (equal); Formal analysis (equal); Methodology (equal); Software (equal); Visualization (equal); Writing – review & editing (equal). **Junfeng Yang:** Funding acquisition (equal); Supervision (equal); Writing – review & editing (equal).

DATA AVAILABILITY

The data that support the findings of this study are available from the corresponding author upon reasonable request.

REFERENCES

Ahmed, P., "Studies of turbulent burning rates and flame structures using 3D optical measurement techniques," Ph.D. dissertation (School of Mechanical Engineering, University of Leeds, 2019).

Abdel-Gayed, R., Bradley, D., and Lawes, M., "Turbulent burning velocities: A general correlation in terms of straining rates," Proc. R. Soc. London A **414**(1847), 389–413 (1987).

Bagdanavicius, A., Bowen, P. J., Bradley, D., Lawes, M., and Mansour, M. S., "Stretch rate effects and flame surface densities in premixed turbulent combustion up to 1.25 MPa," Combust. Flame **162**(11), 4158–4166 (2015).

Bheemul, H. C., Lu, G., and Yan, Y., "Digital imaging-based three-dimensional characterization of flame front structures in a turbulent flame," IEEE Trans. Instrum. Meas. **54**(3), 1073–1078 (2005).

Bradley, D., Gaskell, P., and Gu, X., "Burning velocities, Markstein lengths, and flame quenching for spherical methane-air flames: A computational study," Combust. Flame **104**(1), 176–198 (1996).

Bradley, D., Haq, M., Hicks, R., Kitagawa, T., Lawes, M., Sheppard, C., and Woolley, R., "Turbulent burning velocity, burned gas distribution, and associated flame surface definition," Combust. Flame **133**(4), 415–430 (2003).

Bradley, D., Lawes, M., Liu, K., and Mansour, M. S., "Measurements and correlations of turbulent burning velocities over wide ranges of fuels and elevated pressures," Proc. Combust. Inst. **34**(1), 1519–1526 (2013).

Bradley, D., Lawes, M., and Mansour, M., "Flame surface densities during spherical turbulent flame explosions," Proc. Combust. Inst. **32**(1), 1587–1593 (2009).

Bradley, D., Lawes, M., and Mansour, M. S., "Correlation of turbulent burning velocities of ethanol–air, measured in a fan-stirred bomb up to 1.2 MPa," Combust. Flame **158**(1), 123–138 (2011).

Bradley, D., Lawes, M., and Morsy, M. E., "Measurement of turbulence characteristics in a large scale fan-stirred spherical vessel," J. Turbul. **20**, 195–213 (2019).

Bradley, D., Sheppard, C., Suardjaja, I., and Woolley, R., "Fundamentals of high-energy spark ignition with lasers," Combust. Flame **138**(1), 55–77 (2004).

Bray, K., Domingo, P., and Vervisch, L., "Role of the progress variable in models for partially premixed turbulent combustion," Combust. Flame **141**(4), 431–437 (2005).

Bray, K. N. C. and Peters, N., "Laminar flamelets in turbulent flames," in *Turbulent Reacting Flows*, edited by P. A. Libby and F. A. Williams (Academic Press, London, 1994), pp. 63–114.

Dave, H. L., Mohan, A., and Chaudhuri, S., "Genesis and evolution of premixed flames in turbulence," Combust. Flame **196**, 386–399 (2018).

Driscoll, J. F., "Turbulent premixed combustion: Flamelet structure and its effect on turbulent burning velocities," Prog. Energy Combust. Sci. **34**(1), 91–134 (2008).

Filatyev, S. A., Driscoll, J. F., Carter, C. D., and Donbar, J. M., "Measured properties of turbulent premixed flames for model assessment, including burning velocities, stretch rates, and surface densities," Combust. Flame **141**(1–2), 1–21 (2005).

Gillespie, L., Lawes, M., Sheppard, C., and Woolley, R., "Aspects of laminar and turbulent burning velocity relevant to SI engines," SAE Trans. **109**, 13–33 (2000); available at https://www.jstor.org/stable/44634200.

Halter, F., Chauveau, C., Gökalp, I., and Veynante, D., "Analysis of flame surface density measurements in turbulent premixed combustion," Combust. Flame **156**(3), 657–664 (2009).

Harker, M., Hattrell, T., Lawes, M., Sheppard, C., Tripathi, N., and Woolley, R., "Measurements of the three-dimensional structure of flames at low turbulence," Combust. Sci. Technol. **184**(10–11), 1818–1837 (2012).

Hicks, R., Lawes, M., Sheppard, C., and Whitaker, B., "Multiple laser sheet imaging investigation of turbulent flame structure in a spark ignition engine," SAE Trans. **103**, 1463–1482 (1994); available at http://www.jstor.org/stable/44612436.

Hult, J., Gashi, S., Chakraborty, N., Klein, M., Jenkins, K. W., Cant, S., and Kaminski, C. F., "Measurement of flame surface density for turbulent premixed flames using PLIF and DNS," Proc. Combust. Inst. **31**(1), 1319–1326 (2007).

Hult, J., Omrane, A., Nygren, J., Kaminski, C., Axelsson, B., Collin, R., Bengtsson, P. E., and Aldén, M., "Quantitative three-dimensional imaging of soot volume fraction in turbulent non-premixed flames," Exp. Fluids **33**(2), 265–269 (2002).

Kang, M., Li, X., and Ma, L., "Three-dimensional flame measurements using fiber-based endoscopes," Proc. Combust. Inst. **35**(3), 3821–3828 (2015).

Kroon, D., see https://uk.mathworks.com/matlabcentral/fileexchange/24086-polygon2voxel for "The mathworks file exchange", Surface Mesh Voxelisation Matlab.m File (2016).

Kristensson, E., Berrocal, E., Wellander, R., Ritcher, M., Aldén, M., and Linne, M., "Structured illumination for 3-D Mie imaging and 2-D attenuation measurements in optically dense sprays," Proc. Combust. Inst. **33**(1), 855–861 (2011).

Lawes, M., Sheppard, C. G. W., and Woolley, R., "Three dimensional mapping of turbulent flame fronts," in Ninth Int*ernational* Sym*posium* on Applications of Laser Techniques to Fluid Mechanics*, 13–16 July 1998* (Springer, Lisbon, Portugal, 1998).

Lawes, M., Ormsby, M. P., Sheppard, C. G. W., and Woolley, R., "The turbulent burning velocity of iso-octane/air mixtures," Combust. Flame **159**(5), 1949–1959 (2012).

Lee, G. G., Huh, K. Y., and Kobayashi, H., "Measurement and analysis of flame surface density for turbulent premixed combustion on a nozzle-type burner," Combust. Flame **122**(1–2), 43–57 (2000).

Lipatnikov, A. N. and Chomiak, J., "Turbulent flame speed and thickness: Phenomenology, evaluation, and application in multi-dimensional simulations," Prog. Energy Combust. Sci. **28**(1), 1–74 (2002).

Ma, L., Lei, Q., Capil, T., Hammack, S. D., and Carter, C. D., "Direct comparison of two-dimensional and three-dimensional laser-induced fluorescence measurements on highly turbulent flames," Opt. Lett. **42**(2), 267–270 (2017).

Ma, L., Lei, Q., Ikeda, J., Xu, W., Wu, Y., and Carter, C. D., "Single-shot 3D flame diagnostic based on volumetric laser induced fluorescence (VLIF)," Proc. Combust. Inst. **36**(3), 4575–4583 (2017).

Ma, L., Lei, Q., Wu, Y., Ombrello, T. M., and Carter, C. D., "3D measurements of ignition processes at 20 kHz in a supersonic combustor," Appl. Phys. B **119**(2), 313–318 (2015).

Mantzaras, J., Felton, P. G., and Bracco, F. V., "Three-dimensional visualization of premixed-charge engine flames: Islands of reactants and products; fractal dimensions; and homogeneity," SAE Paper No. 881635, 1988.

Mason, P., Fleischmann, C., Rogers, C., McKinnon, A., Unsworth, K., and Spearpoint, M., "Estimating thermal radiation fields from 3D flame reconstruction," Fire Technol. **45**(1), 1–22 (2009).

Melling, A., "Tracer particles and seeding for particle image velocimetry," Meas. Sci. Technol. **8**(12), 1406 (1997).

Meyer, T. R., Halls, B. R., Jiang, N., Slipchenko, M. N., Roy, S., and Gord, J. R., "High-speed, three-dimensional tomographic laser-induced incandescence imaging of soot volume fraction in turbulent flames," Opt. Express **24**(26), 29547–29555 (2016).

Morley, C., see http://www.gaseq.co.uk for "Gaseq: A chemical equilibrium program for Windows" (2005).

Ng, W. B. and Zhang, Y., "Stereoscopic imaging and reconstruction of the 3D geometry of flame surfaces," Exp. Fluids **34**(4), 484–493 (2003).

Nivarti, G. and Cant, S., "Direct numerical simulation of the bending effect in turbulent premixed flames," Proc. Combust. Inst. **36**(2), 1903–1910 (2017).

Nivarti, G. V. and Cant, R. S., "Scalar transport and the validity of Damköhler's hypotheses for flame propagation in intense turbulence," Phys. Fluids **29**(8), 085107 (2017).

Nwagwe, I. K., Weller, H. G., Tabor, G. R., Gosman, A. D., Lawes, M., Sheppard, C. G. W., and Wooley, R., "Measurements and large eddy simulations of turbulent premixed flame kernel growth," Proc. Combust. Inst. **28**(1), 59–65 (2000).

Nygren, J., Hult, J., Richter, M., Aldén, M., Christensen, M., Hultqvist, A., and Johansson, B., "Three-dimensional laser induced fluorescence of fuel distributions in an HCCI engine," Proc. Combust. Inst. **29**(1), 679–685 (2002).

Peters, N., "The turbulent burning velocity for large-scale and small-scale turbulence," J. Fluid Mech. **384**, 107–132 (1999).

Pole, S. and Cheng, W., "Statistical calculations of spherical turbulent flames," Symp. (Int.) Combust. **21**(1), 1473–1481 (1988).

Steen, W., *Laser Material Processing*, 2nd ed. (Springer-Verlag, London, 1998), pp. 84–87.

Steinberg, A. M., Driscoll, J. F., and Ceccio, S. L., "Measurements of turbulent premixed flame dynamics using cinema stereoscopic PIV," Exp. Fluids **44**(6), 985–999 (2008).

Taubin, G., "A signal processing approach to fair surface design," in *Proceedings of the 5th International Conference on Computer Vision*, Washington DC, USA (IEEE, 1995).

Tanahashi, M., Inoue, S., Shimura, M., Taka, S., Choi, G.-M., and Miyauchi, T., "Reconstructed 3D flame structures in noise-controlled swirl-stabilized combustor," Exp. Fluids **45**(3), 447–460 (2008).

Thorne, B. J. A., *Development of a 3D Laser Imaging System and Its Application in Studies of Turbulent Flame Structure* (University of Leeds, 2017).

Upton, T., Verhoeven, D., and Hudgins, D., "High-resolution computed tomography of a turbulent reacting flow," Exp. Fluids **50**(1), 125–134 (2011).

Wellander, R., Berrocal, E., Kristensson, E., Richter, M., and Aldén, M., "Three-dimensional measurement of the local extinction coefficient in a dense spray," Meas. Sci. Technol. **22**(12), 125303 (2011).

Wellander, R., Richter, M., and Aldén, M., "Time resolved, 3D imaging (4D) of two phase flow at a repetition rate of 1 kHz," Opt. Express **19**(22), 21508–21514 (2011).

Wellander, R., Richter, M., and Aldén, M., "Time-resolved (kHz) 3D imaging of OH PLIF in a flame," Exp. Fluids **55**(6), 1764 (2014).

Yip, B., Lam, J. K., Winter, M., and Long, M. B., "Time-resolved three-dimensional concentration measurements in a gas jet," Science **235**(4793), 1209–1211 (1987).